PROCEEDINGS OF SCIENCE

Simulation of the propagation of CR air shower cores in ice

Simon De Kockere,[a,*] **Krijn de Vries,**[a] **Nick van Eijndhoven**[a] **and Uzair A. Latif**[a]

[a] *IIHE - Vrije Universiteit Brussel (VUB),*
Pleinlaan 2, 1050 Brussels, Belgium

E-mail: simondekockere@gmail.com

We present the results of particle level simulations of the propagation of cosmic ray air shower cores through high-altitude polar ice sheets, using both the COSIKA Monte Carlo code and the Geant4 simulation toolkit. We discuss the general features of the in-ice particle cascade, covering the deposited energy density, the longitudinal development of the shower, and a general parameterization of the radial charge distribution of the cascade front in function of Xmax. We present preliminary calculations of the Askaryan radio emission of the in-ice particle cascades. We find that the core of the air shower dominates the emission during the propagation in the ice, which may mimic an in-ice neutrino-induced particle cascade. Finally, we discuss the feasibility of using RADAR echo techniques to detect the plasma created in the ice by the particle cascade.

9th International Workshop on Acoustic and Radio EeV Neutrino Detection Activities - ARENA2022
7-10 June 2022
Santiago de Compostela, Spain

*Speaker

PoS(ARENA2022)015

1. Introduction

The detection of neutrino interactions in dense media through the observation of radio emission is promising to be a cost efficient method of extending the current sensitivity of neutrino observatories beyond the PeV scale. The particle cascade created by a neutrino interacting in a dense medium will have a net negative charge, leading to Askaryan radio emission. Alternatively, depending on the properties of the medium, the plasma created by the particle cascade can reflect radio waves, making it possible to look for neutrino interactions using RADAR echo techniques [1, 2].

However, besides reducing costs in covering a large detection volume, the long attenuation length of radio emission also means that radio neutrino observatories are typically not very well shielded against background signals. High-energy cosmic rays interacting in the atmosphere will lead to Askaryan and geomagnetic radio emission in air, which can penetrate the medium and reach the radio detectors [3]. At the same time, for observatories located at high altitudes, the energy dense core of the air shower initiated by the cosmic ray will penetrate the medium, starting a particle cascade and creating Askaryan radio emission similar to that of a neutrino-induced cascade. High-energy cosmic rays can therefore form an important background for radio neutrino observatories. However, if well understood, these signals can also be used as an in-situ proof of principle for newly constructed detectors, or as a possible calibration source.

In this work, previously reported in [4], we present the results of particle level simulations of the propagation of cosmic ray air shower cores through high-altitude ice layers, which can be found in polar regions and are currently hosting a number of radio neutrino experiments [5–9]. We will discuss the general features of the in-ice particle cascades, and present the first calculations of the expected Askaryan radio emission. For a discussion on the propagation of the in-air radio emission of cosmic ray air showers into ice, we refer to [10].

2. Simulation setup

A set of proton-induced cosmic ray air showers with different primary particle energies and zenith angles was generated using the *CORSIKA 7.7100* Monte Carlo code [11], using the QGSJETII-04 high energy hadronic interaction model [12], the GHEISHA 2002d low energy hadronic interaction model [13] and a MSIS-E-90 atmospheric model for South Pole on December 31, 1997. Thinning was applied only for showers with primary energies $E_p \geq 10^{17}$ eV on electromagnetic particles falling below $10^{-7}\ E_p$ with a thinning weight smaller than $10^{-7}\ E_p$[GeV]. For electrons, photons and π^0's we used a kinetic energy cut-off of 0.003 GeV. For hadrons (without π^0's) and muons we used a kinetic energy cut-off of 0.3 GeV.

From the *CORSIKA* simulations, for each air shower the position, momentum and arrival time of the secondary particles at an altitude of 2.4 km above sea level was read out and stored. Subsequently, we used the *Geant4 10.5* simulation toolkit [14] to propagate all the secondaries within a radius of 5 m from the core of the particle footprint through ice. The simulated ice consists of different horizontal layers, each with a thickness of 1 cm and a constant density. The density changes per layer, following the ice density profile measured at the Antarctic Taylor Dome ice cap,

$$\rho(z) = 0.460 + 0.468 \cdot \left(1 - e^{-0.02z}\right), \tag{1}$$

with ρ the density in g/cm^3 and z the depth in m. Standard *Geant4* electromagnetic physics is

enabled through the *G4EmStandardPhysics* constructor. We include decay physics of long-lived hadrons and leptons using the *G4DecayPhysics* constructor, and added radioactive decay physics via the *G4RadioactiveDecayPhysics* constructor. Instead of using hard kinetic energy cut-offs, *Geant4* uses production cut-off lengths. A secondary particle will only be created during the simulation if it will be able to travel a distance larger then its corresponding production cut-off length. We used a cut-off length of 1 mm for gammas, electrons, positrons and protons.

We included the end-point formalism in the *Geant4* framework to calculate the radio emission of the in-ice particle cascade [15]. This formalism is also used in *CoREAS*, which calculates the radio emission of air showers simulated by the *CORSIKA* Monte Carlo code, and agrees well with experimental results [16]. The same approach was followed for the SLAC T-510 experiment, of which we used the code as an example [17, 18].

The end-point formalism calculates the electric field created in a point-like observer for a charged particle following an arbitrary path in a medium, by dividing the path into small segments. For each segment the contribution to the total electric field is calculated by assuming that the charge got instantly accelerated from rest to its constant segment velocity β^* at the start point of the segment, and instantly decelerated back to rest at the end point of the segment. The contribution to the total electric field is then given by

$$\vec{E}_{\pm}(\vec{x}, t) = \pm \frac{1}{\Delta t} \frac{q}{c} \left(\frac{\hat{r} \times [\hat{r} \times \vec{\beta}^*]}{|1 - n\vec{\beta}^* \cdot \hat{r}|R} \right), \tag{2}$$

with Δt the sampling time interval of the observer, q the charge of the particle, $\hat{r}$ the direction from the start/end point towards the observer, R the distance between the start/end point and the observer and n the index of refraction of the medium. The plus sign corresponds to the emission at the start point and the minus sign to the emission at the end point.

This formalism in principle only works in a medium with constant index of refraction n. The detection modules of radio neutrino observatories are typically located in the upper layers of natural ice, where n is expected to change significantly as a function of depth. Assuming a constant index of refraction might thus be an oversimplification. In [19], it is shown that by including ray tracing Eq. 2 still holds, when interpreting $\hat{r}$ as the launching direction of the ray, evaluating n at the launching point of the ray and rotating the electric field in the plain of the ray so it is perpendicular to the ray at the observer. This approach will be included in future work. In this work we will use a fixed value of $n = 1.52$.

3. Simulation results

For illustration, we will primarily show results for a simulated air shower initiated by a 10^{17} eV proton primary entering the atmosphere at a zenith angle $\theta = 0°$. It reaches a maximum number of positrons and electrons at a shower depth of $X_{max} = 680$ g/cm^2, with shower depth defined as the density of the medium integrated along the path of the shower. As can be seen in e.g. [20], this is a good average value for X_{max} for a proton induced air shower with the given primary energy.

Fig. 1 summarizes two main features of the simulated air shower. Fig. 1a shows the longitudinal particle distribution per particle component. At the altitude of the ice surface, the high-energy cosmic ray air shower reaches its maximum number of particles. The electromagnetic component (gamma rays, positrons and electrons) outnumber the muonic and hadronic components by several

orders of magnitude. Fig. 1b shows the total energy per particle component within a given radius at the altitude of the ice surface. The shower has a very energy dense core, with roughly 15% of the primary proton's energy concentrated within a radius of 100 cm. Interestingly, we can therefore expect the in-ice particle cascade to be very similar to that of a neutrino-induced particle cascade, as its development will be mainly determined by this energy-dense core.

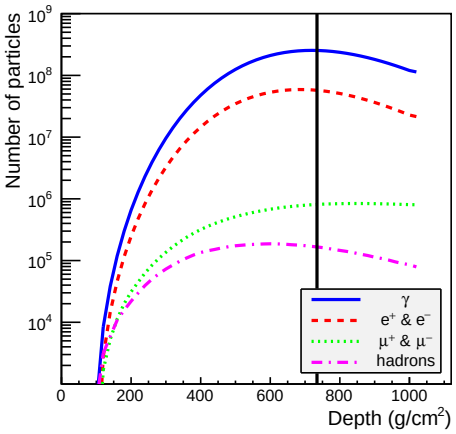

(a) The number of particles per particle component reaching a given depth. The black vertical line indicates the altitude of 2.4 km (734 g/cm^2).

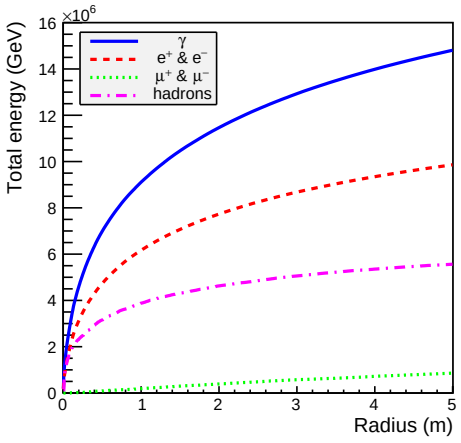

(b) The total energy within a given radius per particle component at an altitude of 2.4 km.

Figure 1: Two main features of the simulated air shower. Fig. taken from [4].

3.1 Deposited energy in the ice

Fig. 2 shows the energy deposited in the ice within a vertical 1-cm wide slide through the center of the particle shower, calculated using the *Geant4* module for the simulated air shower. Here we again clearly see the high-energetic shower core dominating during the propagation of the particle cascade through the ice. Close to the core the average energy of the electromagnetic particles is well above the critical energy for showering ($\sim$ 80 MeV), and we can therefore see the core growing, reaching a maximum a few meters below the ice surface. At larger radii the cascade is simply dying out.

3.2 Longitudinal shower development

Fig. 4 gives the longitudinal shower development of the simulated air shower, showing the number of particles in the full radial extend of the cascade as a function of depth. The dashed lines show the case where the shower propagates through air reaching sea level. The solid lines show the case where the shower propagates through the ice layer at 2.4 km above sea-level, using the above-mentioned *CORSIKA* kinetic energy cut-offs during the *Geant4* simulation. As shown, the propagation through ice does not influence the development of the electromagnetic part, which can therefore be described using parameterizations already available in literature, e.g. the Gaisser-Hillas parameterization [21]. Due to the higher density, charged pion interaction is favored over their decay in ice, slowing down the decline of the hadronic component and suppressing the muonic component.

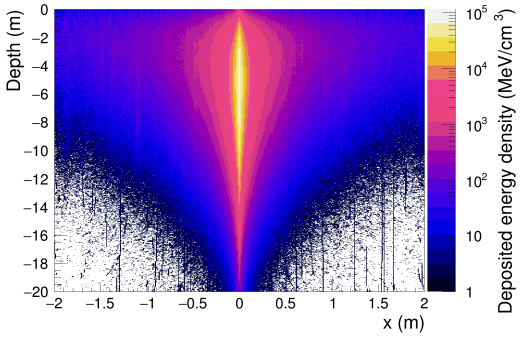

Figure 2: The deposited energy density within a vertical 1-cm wide slice going through the center of the simulated shower. Fig. taken from [4].

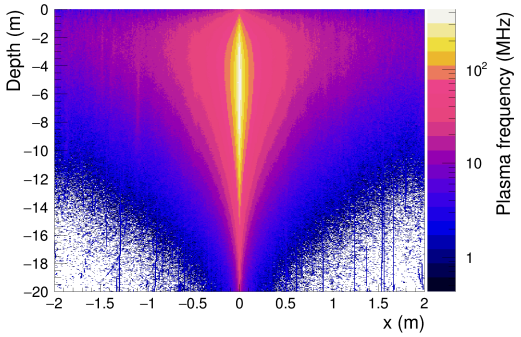

Figure 3: The estimated plasma frequency of the plasma created in ice by the simulated shower, as explained in Sec. 3.5. Fig. taken from [4].

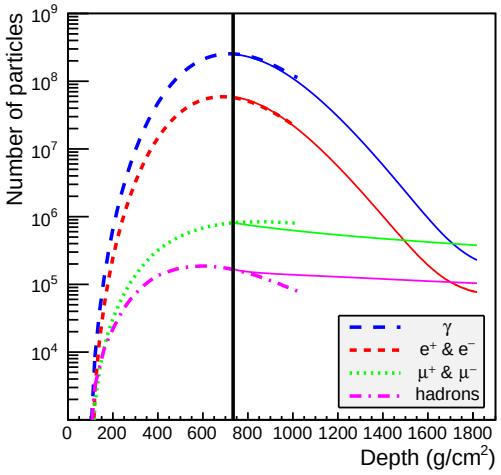

Figure 4: The total number of particles in the simulated air shower in function of depth. The dashed lines show the case where the shower propagates through air, reaching sea level. The solid lines show the case where the shower propagates through ice at 2.4 km above sea-level, indicated by the black vertical line, using the above-mentioned *CORSIKA* kinetic energy cut-offs during the *Geant4* simulation. Fig. taken from [4].

3.3 Lateral charge distribution

In Fig. 5a we show the lateral charge distribution $w_1(r)$ for the simulated shower at different stages of the cascade development in the ice, indicated by the depth with respect to the ice surface of the cascade front. By definition, $w_1(r)dr$ gives the number of charges within the radial interval $[r, r + dr]$, normalized such that $\int_0^{R_0} w_1(r)dr = 1$. Here we use $R_0 = 0.2$ m, as we are mostly interested in the region close to the shower core. As the longitudinal dimension of the in-ice cascade is very small, this essentially describes the cascade front particle distribution. As mentioned above, close to the core the in-ice cascade is still growing, while at larger radii it is dying out, which is reflected in the $w_1(r)$ distribution narrowing during the propagation. Around a cascade front depth of 450 g/cm^2 a stable distribution is found.

To account for shower-to-shower fluctuations we constructed a proton shower simulation set, with primary energies varying from 10^{16} eV up to 10^{18} eV in half decade steps, and using zenith

angles of 0°, 15° and 30°, resulting in a total of 150 showers. Next, we calculated the average $w_1(r)$ distributions at a shower front depth of 450 g/cm^2 for showers with a similar X_{max} value, ignoring their primary energies and zenith angles. This is shown in Fig. 5b. A clear trend between X_{max} and the shape of the distributions can be seen. Showers with a high X_{max} value will be more concentrated around the core when reaching the ice surface, resulting in a sharper $w_1(r)$ distribution. We found that the average $w_1(r)$ distributions can be well described with the analytical expression

$$W(r) = \frac{1}{A}\sqrt{r}e^{-(r/b)^c}, \tag{3}$$

with b and c two fit parameters depending on X_{max} of the showers and A a normalization factor given by

$$A = \frac{b^{3/2}}{c}\left\{\Gamma\left(\frac{3}{2c}\right) - \Gamma\left(\frac{3}{2c}, \left(\frac{R_0}{b}\right)^c\right)\right\},$$

where $\Gamma(x)$ is the gamma function and $\Gamma(a,x)$ the upper incomplete gamma function. The parameters b and c for a shower front depth of 450 g/cm^2 in function of X_{max} are shown in Fig. 6, using the mean X_{max} value for each interval. Also shown are linear fits which can be used to reconstruct the $w_1(r)$ distribution for a shower given using Eq. 3 and its X_{max} value.

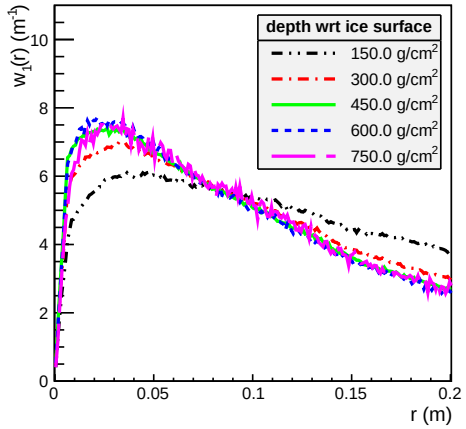

(a) The $w_1(r)$ distributions for the example simulated shower at different stages of the cascade development in the ice, indicated by the depth with respect to the ice surface of the cascade front, going from 150 g/cm^2 (3.2 m) up to 750 g/cm^2 (14.4 m).

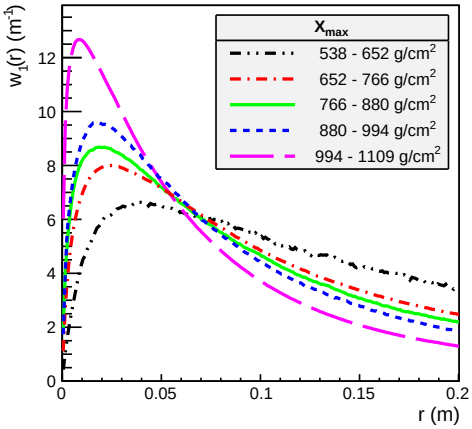

(b) The average $w_1(r)$ distributions at a cascade front depth of 450 g/cm^2 with respect to the ice surface. The text box of the plot indicates the X_{max} intervals for which the corresponding average w_1 distribution was calculated.

Figure 5: The $w_1(r)$ distribution for the example simulated air shower, and the average $w_1(r)$ distributions for the simulation set. Fig. taken from [4].

3.4 Askaryan radio emission

As outlined previously we use the end-point formalism to calculate the radio emission from the in-ice particle cascade. We use a coordinate system where the x- and y-axis are horizontal to the ice surface, and the z-axis is pointing upwards perpendicular to the ice surface. Fig. 7 shows the electric field components for the simulated shower as seen by a point-like antenna at a distance 100 m from the point of impact of the shower core with the ice surface, using different viewing

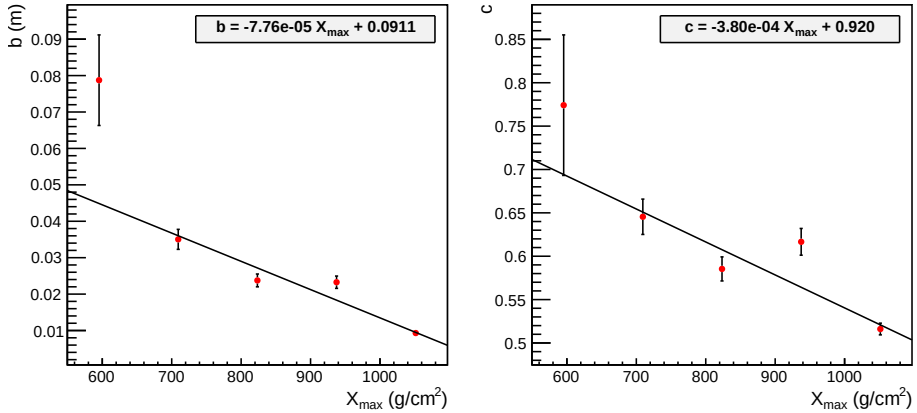

Figure 6: The b and c parameters of Eq. 3 in function of X_{max} for a cascade front depth of 450 g/cm^2 with respect to the ice surface. The error bars are derived from the standard deviations on the average $w_1(r)$ distributions. Fig. taken from [4].

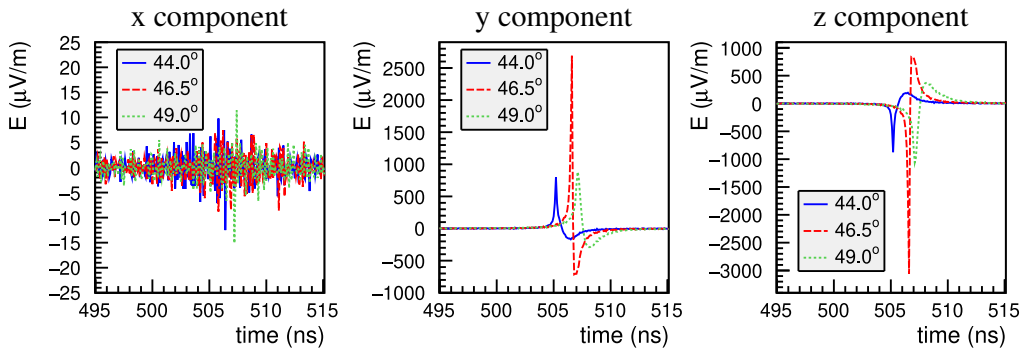

Figure 7: The electric field components from the in-ice Askaryan radio emission of the simulated shower for a point-like antenna at a distance 100 m from the point of impact of the shower core with the ice surface, at different viewing angles. The x-coordinate of the antenna is fixed at x = 0. The viewing angle is clockwise with respect to the shower axis, measured from the point of impact on the ice surface. Time $t = 0$ refers to the moment when the shower core enters the ice. Fig. taken from [4].

angles. The x-coordinate of the antenna is fixed at $x = 0$. We find a radially polarized bipolar signal, a characteristic feature of Askaryan radio emission, well above typical detection thresholds. The value $n = 1.52$ corresponds to a Cherenkov angle of 49.0°, yet we find the strongest signal at an angle of 46.5°. This shift towards a smaller viewing angle is to be expected, as it is defined with respect to the point of impact on the ice surface, while most of the radiation is emitted deeper into the ice. This also explains the arrival time differences for the different viewing angles.

3.5 RADAR echo detection

To characterize the capability of the plasma created in the ice by air shower core to reflect radio emission, we calculate the plasma frequency ω_p, which can be expressed as

$$\omega_p = 8980\sqrt{n_q\,[\mathrm{cm}^{-3}]}\ \mathrm{Hz}, \tag{4}$$

with n_q the free charge density of the plasma [1]. We can estimate n_q from the deposited energy density ρ_E in ice as $n_q = \rho_E/(50\text{ eV})$. Fig. 3 shows ω_p for the simulated shower, where reaching values of 100 MHz and above. This suggests that the plasma is able to reflect radio emission. For more detail on this topic, we refer to the works presented in [22–25].

References

[1] K. D. de Vries, K. Hanson, and T. Meures, Astropart. Phys. **60**, 25 (2015), arXiv:1312.4331.
[2] S. Prohira, K. D. de Vries, P. Allison, J. Beatty, D. Besson, A. Connolly, et al., Phys. Rev. Lett. **124**, 091101 (2020), arXiv:1910.12830.
[3] Krijn D. de Vries, Stijn Buitink, Nick van Eijndhoven, Thomas Meures, Aongus O'Murchadha, Olaf Scholten, Astropart. Phys. **74** (2016) 96-104, arXiv:1503.02808.
[4] S. De Kockere, K. D. de Vries, N. van Eijndhoven, U. A. Latif, Phys. Rev. D **106**, 043023 (2022), arXiv:2202.09211.
[5] ANITA collaboration, Astropart. Phys. **32**, 10 (2009), arXiv:0812.1920.
[6] ARA collaboration, Astropart. Phys. **35**, 457 (2012), arXiv:1105.2854.
[7] ARIANNA collaboration, IEEE Trans. Nucl. Sci. **62**, 2202 (2015), arXiv:1410.7369.
[8] RNO-G collaboration, JINST **16**, P03025 (2021), arXiv:2010.12279.
[9] PUEO collaboration, JINST **16**, P08035 (2021), arXiv:2010.02892.
[10] U. A. Latif, S. Buitink, S. De Kockere, K. D. de Vries, T. Huege, D. Van den Broeck, PoS **ARENA2022**, 016 (2022).
[11] D. Heck, J. Knapp, J. Capdevielle, G. Schatz, and T. Thouw, FZKA **6019** (1998).
[12] S.Ostapchenko, PRD **83** (2011) 014018
[13] H. Fesefeldt, Report PITHA-85/02 (1985), RWTH Aachen, available at http://cds.cern.ch/record/162911/files/CM-P00055931.pdf
[14] S. Agostinelli et al., Nucl. Instrum. Methods Phys. Res. A **506**, 250 (2003).
[15] C. W. James, H. Falcke, T. Huege, and M. Ludwig, Physical Review E **84**, 056602 (2011), arXiv:1007.4146.
[16] A. Nelles, S. Buitink, H. Falcke, J. Hörandel, T. Huege, and P. Schellart, Astroparticle Physics **60**, 13 (2014), arXiv:1402.2872.
[17] A. Zilles, *Emission of Radio Waves in Particle Showers: Validation of microscopic simulations with the SLAC T-510 experiment and their potential in the future Square Kilometer Array* (Springer, 2017).
[18] K. Bechtol, K. Belov, K. Borch, P. Chen, J. Clem, P. Gorham, et al., Phys. Rev. D **105**, 063025 (2022), arXiv:2111.04334.
[19] D. Van den Broeck, S. Buitink, K. D. de Vries, T. Huege, U. A. Latif, PoS **ARENA2022**, 020 (2022).
[20] S. Buitink et al., Nature **531**, 70 (2016), arXiv:1603.01594.
[21] T. Gaisser and A. Hillas, Proc. 15th ICRC, Bulgarian academy of sciences, Plovdiv (Bulgaria) **8**, 353 (1977).
[22] S. Prohira, K. D. de Vries, P. Allison, J. Beatty, D. Besson, A. Connolly, et al., Phys. Rev. D **104**, 102006 (2021), arXiv:2104.00459.
[23] R. Stanley et al. (RET collaboration), PoS **ARENA2022**, 009 (2022).
[24] V. Lukic et al. (RET collaboration), PoS **ARENA2022**, 010 (2022).
[25] E. Huesca Santiago et al. (RET collaboration), PoS **ARENA2022**, 017 (2022).